Validation of the GreenX library time-frequency component for efficient *GW* and RPA calculations

Maryam Azizi [●],[1] Jan Wilhelm [●],[2] Dorothea Golze [●],[3] Francisco A. Delesma [●],[3,4] Ramón L. Panadés-Barrueta [●],[3]
Patrick Rinke,[4] Matteo Giantomassi [●],[1] and Xavier Gonze [●][1]

[1]*Université catholique de Louvain, Chemin des étoiles 8, bte L07.03.01, B-1348 Louvain-la-Neuve, Belgium*
[2]*Institute of Theoretical Physics and Regensburg Center for Ultrafast Nanoscopy (RUN), University of Regensburg, Regensburg 93059, Germany*
[3]*Faculty for Chemistry and Food Chemistry, Technische Universität Dresden, 01062 Dresden, Germany*
[4]*Department of Applied Physics, Aalto University, FI-02150 Espoo, Finland*

Electronic structure calculations based on many-body perturbation theory [e.g., *GW* or the random-phase approximation (RPA)] require function evaluations in the complex time and frequency domain, for example, inhomogeneous Fourier transforms or analytic continuation from the imaginary axis to the real axis. For inhomogeneous Fourier transforms, the time-frequency component of the GreenX library provides time-frequency grids that can be utilized in low-scaling RPA and *GW* implementations. In addition, the adoption of the compact frequency grids provided by our library also reduces the computational overhead in RPA implementations with conventional scaling. In this paper, we present low-scaling *GW* and conventional RPA benchmark calculations using the GreenX grids with different codes (FHI-aims, CP2K, and ABINIT) for molecules, two-dimensional materials and solids. Very small integration errors are observed when using 30 time-frequency points for our test cases, namely $< 10^{-8}$ eV/electron for the RPA correlation energies, and $\leqslant 10$ meV for the *GW* quasiparticle energies.

I. INTRODUCTION

GW calculations [1] have become part of the standard toolbox in computational condensed-matter physics for the calculation of photoemission and optoelectronic spectra of molecules and solids [2–7]. Recent highlights include a wide array of advancements, such as the application of *GW* to deep core excitations [8–16], *GW* studies of two-dimensional (2D) materials [17–24] and metal-halide perovskites [25–30]. Additionally, research has delved into exploring excited-state potential energy surfaces from *GW*+Bethe-Salpeter [31–33] and applying the *GW* methodology in magnetic fields [34–36]. Relativistic *GW* schemes with two-component spinors have recently gained attention to treat spin-orbit coupling [37–40]. Furthermore, machine learning models have been developed for quasiparticle energies [41–47] and studies have investigated electron dynamics from Green's functions [48–56]. Additionally, there have been focused studies related to *GW* itself, like benchmarking the accuracy of the *GW* method [57–60] and benchmarking the numerical precision of *GW* implementations [61–67].

For the calculation of total energies, the random phase approximation (RPA) [68,69] offers several appealing features. It includes long-range dispersion interactions and dynamic electronic screening, that are absent from density functionals like the local density approximation [70] or the generalized gradient approximation (GGA) [71], and even absent from hybrid functionals admixing GGAs and exact exchange [72]. Despite its large computational cost, RPA has been applied to a wide range of systems, from zero to three dimensions [73–79]. Recent highlights include RPA forces [80–85], RPA-based interatomic potentials [86–88], and applications to complex systems such as phase transitions in solid hydrogen [89] and cesium-lead-triiodide [90], oxychlorinated platinum complexes [91], chromophores [92], and perhalogenated benzene clusters [93].

Several algorithmic bottlenecks, however, render *GW* and RPA calculations challenging, especially for complex or disordered systems with large simulations cells. In their conventional implementations, the computational cost increases with the fourth power of the system size N_{at}, $\mathcal{O}(N_{at}^4)$. As a consequence, conventional *GW* calculations are usually limited to systems with a few hundred of atoms [41,94]. There are many approaches to make larger system sizes tractable, which include massively parallel implementations over physically motivated approximations to novel numerical methods. Efficient parallelization schemes were developed for execution on more than 10 000 CPU cores [94–98] and first algorithms have been already proposed for the new generation of heavily GPU-based (pre)exascale supercomputers [99–101]. An example for more physically motivated developments are *GW* embedding schemes, where a small part of the system is calculated at the *GW* level and the surrounding medium is treated at a lower level of theory [102–106].

In order to reduce the computational cost of *GW* and RPA calculations, an alternative path relies on low-scaling algorithms that allow one to tackle larger and more realistic systems. Low-scaling *GW* methods can be constructed using space-local representations and imaginary time-frequency transforms [107] so that cubic scaling of the computational cost in the system size N_{at} is achieved, $\mathcal{O}(N_{at}^3)$, instead of quartic scaling $\mathcal{O}(N_{at}^4)$ of conventional *GW* algorithms [94].

Several cubic-scaling algorithms have been recently implemented, e.g., using a plane-wave basis set and real-space grids [108–111] or using atom-orbital-like basis functions [24,39,112–117]. Several key steps of these algorithms, like computing the polarizability, scale quadratically or even linearly [118,119] so that the observed scaling is often close to quadratic [24,112,113]. All of these *GW* algorithms have in common that three Fourier transforms between imaginary time and imaginary frequency and vice versa need to be performed numerically. The total computational cost increases linearly with the number of time and frequency grid points, which makes it attractive to construct numerically accurate grids with a minimal number of grid points. Time and frequency grids can be constructed from solving an optimization problem, either using least-squares optimization [120–122] or the minimax approximation [108,110,123]. The minimax approximation is referred to as the best approximation, in the sense that it minimizes the maximum error of the numerical integration [108,124]. We have recently published time-frequency grids generated from the minimax approximation in the open-source GreenX library [125,126], which is interfaced to the electronic structure codes FHI-aims [127], CP2K [128], and ABINIT [129,130].

In this paper, we use minimax grids from the GreenX library [125,126] together with the three codes to perform accuracy benchmark calculations for *GW* quasiparticle energies and RPA correlation energies. Our goal is to examine the validity of the grids for a wide range of finite and extended systems. We aim to demonstrate that the GreenX grids are reliable for low-scaling algorithms, and that also conventional RPA implementations with quartic scaling benefit from our library.

The article is organized as follows: In Sec. II, we discuss the low-scaling *GW* and RPA algorithm in imaginary time and imaginary frequency. Section III describes the minimax formalism for creating imaginary-time and imaginary-frequency grids. We finally present low-scaling *GW* and conventional-scaling RPA benchmark calculations on molecules, 2D materials and solids, where computational details are given in Sec. IV. We present and discuss the results in Sec. V and provide our conclusions in Sec VI.

II. RPA AND *GW* METHODOLOGY IN IMAGINARY TIME AND FREQUENCY

In this section, we define the Green's functions, susceptibility and Fourier transformations from imaginary time to imaginary frequency and vice versa, which are then used to compute the RPA correlation energy and *GW* quasiparticle energies. In the entire paper, we consider a nonmagnetic system with scalar wave function and we consequently drop the spin index.

Within the adiabatic-connection fluctuation-dissipation formalism [73,74,131–133], the RPA correlation energy can be written as

$$E_c^{\text{RPA}} = \int_0^\infty \frac{d\omega}{2\pi} \text{Tr}\{\ln[1 - \chi^0(i\omega)V] + \chi^0(i\omega)V\}, \quad (1)$$

where χ^0 stands for the RPA irreducible independent-particle susceptibility (or irreducible density response) evaluated on

the imaginary frequency axis ($i\omega$ with ω being real) and V denotes the frequency-independent Coulomb interaction. Spatial arguments have been omitted for brevity. "Tr" is the trace over such spatial arguments. The RPA susceptibility is also an ingredient for the *GW* self-energy.

In the Adler-Wiser formula [134,135], the noninteracting susceptibility in the imaginary-frequency domain can be obtained as follows:

$$\chi^0(\mathbf{r}, \mathbf{r}', i\omega) = \sum_j^{\text{occ}} \sum_a^{\text{unocc}} \psi_a^*(\mathbf{r}')\psi_j(\mathbf{r}')\psi_j^*(\mathbf{r})\psi_a(\mathbf{r})$$
$$\times \frac{2(\epsilon_j - \epsilon_a)}{\omega^2 + (\epsilon_j - \epsilon_a)^2}, \quad (2)$$

where indices j and a refer to occupied and unoccupied Kohn-Sham (KS) or Hartree-Fock states [$\psi(\mathbf{r})$] with energies ϵ. The computational cost required to compute Eq. (2) in the frequency domain scales as $\mathcal{O}(N_{\text{at}}^4)$, since the number of states (j and a indices) and discretized real space points (**r** and **r**′) scale linearly with system size N_{at}. This is a significant bottleneck, which can be reduced by invoking the low-scaling space-time approach [107].

By Fourier transforming Eq. (2) in imaginary time ($i\tau$), the two summations decouple,

$$\hat{\chi}^0(\mathbf{r}, \mathbf{r}', i\tau) = -\sum_j^{\text{occ}} \psi_j(\mathbf{r}')\psi_j^*(\mathbf{r})e^{\epsilon_j|\tau|}$$
$$\times \sum_a^{\text{unocc}} \psi_a^*(\mathbf{r}')\psi_a(\mathbf{r})e^{-\epsilon_a|\tau|}. \quad (3)$$

A circumflex accent is used to denote Fourier transformed functions of the imaginary time. For completeness, we mention here that Eq. (3) is equivalent to expressing χ^0 as a product of two noninteracting Green's functions,

$$\hat{\chi}^0(\mathbf{r}, \mathbf{r}', i\tau) = \hat{G}(\mathbf{r}, \mathbf{r}', i\tau)\hat{G}(\mathbf{r}', \mathbf{r}, -i\tau), \quad (4)$$

with

$$\hat{G}(\mathbf{r}, \mathbf{r}', i\tau)$$
$$= \begin{cases} \sum_j^{\text{occ}} \psi_j(\mathbf{r})\psi_j^*(\mathbf{r}')e^{-|(\epsilon_j - \epsilon_{\text{F}})\tau|} & \text{for } \tau < 0, \\ -\sum_a^{\text{unocc}} \psi_a^*(\mathbf{r})\psi_a(\mathbf{r}')e^{-|(\epsilon_a - \epsilon_{\text{F}})\tau|} & \text{for } \tau > 0, \end{cases} \quad (5)$$

where ϵ_{F} is the Fermi energy. For keeping the notation short and in line with the convention used in Ref. [110], we have omitted the prefactor, the imaginary unit, from the Green's function unlike in our recent presentation of the GreenX library [126]. The computational cost of the Green's function scales cubically in N_{at} and so does $\hat{\chi}^0$. The space-time approach therefore saves one order in N_{at} compared to the aforementioned Adler-Wiser formalism.

With Fourier transformations χ^0 and χ can be switched between (imaginary) time and frequency,

$$f(\mathbf{r}, \mathbf{r}', i\omega) = \int_{-\infty}^{+\infty} e^{-i\omega\tau}\hat{f}(\mathbf{r}, \mathbf{r}', i\tau)d\tau,$$
$$\hat{f}(\mathbf{r}, \mathbf{r}', i\tau) = \frac{1}{2\pi}\int_{-\infty}^{+\infty} e^{i\omega\tau}f(\mathbf{r}, \mathbf{r}', i\omega)d\omega. \quad (6)$$

Since both susceptibilities are even functions in frequency and time [$\chi^0(i\omega) = \chi^0(-i\omega)$ and $\hat{\chi}^0(i\tau) = \hat{\chi}^0(-i\tau)$], these transforms simplify to cosine transformations,

$$
\begin{aligned}
\chi^0(\mathbf{r}, \mathbf{r}', i\omega) &= \int_{-\infty}^{+\infty} e^{i\omega\tau}\, \hat{\chi}^0(\mathbf{r}, \mathbf{r}', i\tau) d\tau \\
&= \int_{-\infty}^{+\infty} (\cos(\omega\tau) + i\sin(\omega\tau))\, \hat{\chi}^0(\mathbf{r}, \mathbf{r}', i\tau) d\tau \\
&= \int_{-\infty}^{+\infty} \cos(\omega\tau)\, \hat{\chi}^0(\mathbf{r}, \mathbf{r}', i\tau) d\tau \\
&= 2 \int_{0}^{+\infty} \cos(\omega\tau)\, \hat{\chi}^0(\mathbf{r}, \mathbf{r}', i\tau) d\tau.
\end{aligned}
\tag{7}
$$

After a Fourier transforming χ to imaginary frequency, the dielectric function can be calculated in the imaginary-frequency domain as

$$
\epsilon(\mathbf{r}, \mathbf{r}', i\omega) = \delta(\mathbf{r}, \mathbf{r}') - \int d\mathbf{r}''\, V(\mathbf{r}, \mathbf{r}'')\chi^0(\mathbf{r}'', \mathbf{r}', i\omega). \tag{8}
$$

The screened Coulomb interaction W is then given by

$$
W(\mathbf{r}, \mathbf{r}', i\omega) = \int d\mathbf{r}''\epsilon^{-1}(\mathbf{r}, \mathbf{r}'', i\omega)V(\mathbf{r}'', \mathbf{r}') \tag{9}
$$

and cosine transformed into the time domain,

$$
\begin{aligned}
\hat{W}(\mathbf{r}, \mathbf{r}', i\tau) &= \frac{1}{2\pi} \int_{-\infty}^{+\infty} e^{i\omega\tau}\, W(\mathbf{r}, \mathbf{r}', i\omega)\, d\omega, \\
&= \frac{1}{\pi} \int_{0}^{+\infty} \cos(\omega\tau)\, W(\mathbf{r}, \mathbf{r}', i\omega)\, d\omega.
\end{aligned}
\tag{10}
$$

The self-energy follows as a product with the Green's function

$$
\hat{\Sigma}(\mathbf{r}, \mathbf{r}', i\tau) = -\hat{G}(\mathbf{r}, \mathbf{r}', i\tau)\hat{W}(\mathbf{r}, \mathbf{r}', i\tau). \tag{11}
$$

The quasiparticle energies are then obtained from the matrix elements of the self-energy with respect to the single-particle wave functions of the corresponding states after Fourier transforming the self-energy from imaginary time to imaginary frequency. Since the self-energy is neither an odd nor an even function, both cosine and sine transformations are needed [110],

$$
\Sigma(i\omega) = -\int_{\infty}^{\infty} d\tau\, \hat{G}(i\tau)\hat{W}(i\tau)e^{i\omega t} \tag{12}
$$

$$
= 2 \int_{0}^{\infty} d\tau\, \hat{\Sigma}^c(i\tau) \cos(\omega\tau) \tag{13}
$$

$$
+ 2i \int_{0}^{\infty} d\tau\, \hat{\Sigma}^s(i\tau) \sin(\omega\tau), \tag{14}
$$

where

$$
\hat{\Sigma}^c(i\tau) = -\tfrac{1}{2}[\hat{G}(i\tau) + \hat{G}(-i\tau)]\hat{W}(i\tau), \tag{15}
$$

$$
\hat{\Sigma}^s(i\tau) = -\tfrac{1}{2}[\hat{G}(i\tau) - \hat{G}(-i\tau)]\hat{W}(i\tau). \tag{16}
$$

This is the last step in the low-scaling algorithm, which will then be followed by the calculation of the quasiparticle energy using analytic continuation [2,110,113].

III. MINIMAX TIME AND FREQUENCY INTEGRATION GRIDS

In this section, we describe the generation of time and frequency integration grids using the minimax approximation, following the procedure from Ref. [108] (Secs. III A – III C) and partially Ref. [110] (Sec. III D).

A. Analytical form of functions in time and frequency

In Sec. II we have discussed that the computation of the susceptibility in the imaginary time domain scales favorably. However, the subsequent time-frequency Fourier transform of such a function is challenging if performed numerically. Equation (2) in the frequency domain is the exact (cosine) Fourier transform of Eq. (3), in the time domain. In a numerical approach, Eq. (3) has to be evaluated for a finite set of time points, where the set should be as small as possible for an efficient algorithm. However, the functions introduced in the previous section in the imaginary time and frequency domains usually have long tails and very localized features. As such, a usual fast Fourier transform, with homogeneously spaced integration grids, would need numerous sampling points. Instead, a nonuniform Fourier transform (actually cosine and sine transforms) would yield a reduction by more than one order of magnitude in the computational requirements (both CPU time and memory).

The problem is thus to find the "best set" of time points, and associated weights, to discretize the integral in Eq. (7). Similarly, the inverse transform Eq. (10) from frequency to time has to be performed on an equivalently "best set" of frequency points. One option for defining a "best set" of points and weights is to exploit the functional form of the frequency dependence of Eq. (2), and the time dependence of Eq. (3). For simplicity [108], we single out the frequency and time dependence of Eqs. (2) and (3),

$$
\chi(i\omega) = \sum_{\mu} \chi_{\mu}\phi_{\omega}(x_{\mu}), \tag{17}
$$

$$
\hat{\chi}(i\tau) = \sum_{\mu} \chi_{\mu}\hat{\phi}_{\tau}(x_{\mu}), \tag{18}
$$

thanks to the auxiliary functions

$$
\phi_{\omega}(x) := \frac{2x}{x^2 + \omega^2}, \tag{19}
$$

$$
\hat{\phi}_{\tau}(x) := e^{-x|\tau|}, \tag{20}
$$

where μ in Eqs. (17) and (18) runs over the occupied-state index j and the unoccupied-state index a, x_{μ} is the energy difference between occupied and unoccupied states ($x_{\mu} = \epsilon_a - \epsilon_j > 0$), and $\chi_{\mu} = \psi_a^*(\mathbf{r}')\psi_j(\mathbf{r}')\psi_j^*(\mathbf{r})\psi_a(\mathbf{r})$ denotes the elements of the susceptibility matrix in the transition space. Note that $\epsilon_{\min} \leqslant x_{\mu} \leqslant \epsilon_{\max}$, with $\epsilon_{\min}$ being the energy or band gap and $\epsilon_{\max}$ the maximum energy difference.

B. Time and frequency integration for the direct MP2 correlation energy

We make use of the functional forms expressed in Eqs. (17) and (18) in the following way [108]: In Eq. (1), for the RPA correlation energy, the function $\ln(1 - x) + x = -x^2/2 - x^3/3 - \dots$ is appearing. Thus, the lowest order in the RPA correlation energy expansion in $\chi(i\omega)V$ is given by the second

order,

$$E_c^{(2)} = -\frac{1}{4\pi} \int_0^\infty d\omega \, \text{Tr}\{(\chi(i\omega)V)^2\} \tag{21}$$

$$= -\frac{1}{4} \sum_{\mu\mu'} \text{Tr}\{\chi_\mu V \chi_{\mu'} V\} \frac{1}{\pi} \int_0^\infty d\omega \, \phi_\omega(x_\mu) \phi_\omega(x_{\mu'}), \tag{22}$$

which is precisely the direct second-order Møller-Plesset correlation energy (MP2) [120]. Inserting the Fourier transform (7) of $\chi(i\omega)$ into Eq. (21), we obtain

$$E_c^{(2)} = -\frac{1}{2} \int_0^\infty d\tau \, \text{Tr}\{(\hat{\chi}(i\tau)V)^2\} \tag{23}$$

$$= -\frac{1}{4} \sum_{\mu\mu'} \text{Tr}\{\chi_\mu V \chi_{\mu'} V\} 2 \int_0^\infty d\tau \, \hat{\phi}_\tau(x_\mu) \hat{\phi}_\tau(x_{\mu'}). \tag{24}$$

Equations (22) and (24) evaluate to [108,120]

$$E_c^{(2)} = -\frac{1}{4} \sum_{\mu\mu'} \text{Tr}\{\chi_\mu V \chi_{\mu'} V\} \frac{1}{x_\mu + x_{\mu'}}. \tag{25}$$

C. Constructing minimax time and frequency grids

Equations (21)–(25) are an ideal starting point to construct time and frequency grids. The frequency integral in Eq. (22) is discretized by a frequency grid

$$\vec{\omega} = \{\omega_k\}_{k=1}^N \tag{26}$$

and integration weights

$$\vec{\gamma} = \{\gamma_k\}_{k=1}^N, \tag{27}$$

where N is the number of integration points. Following Kaltak *et al.* [108], the grid generation is simplified by restricting Eqs. (22) and (25) to identical transition energies $x_\mu = x_{\mu'}$. We require that the discretized frequency integral of Eq. (22) is as close as possible to the exact result $1/(2x_\mu)$ from Eq. (25), i.e., the error function

$$\eta_{\vec{\gamma}, \vec{\omega}}(x) = \frac{1}{2x} - \frac{1}{\pi} \sum_{k=1}^N \gamma_k \phi_{\omega_k}^2(x), \tag{28}$$

is minimized with respect to $\vec{\omega}$ and $\vec{\gamma}$.

Similarly, the time integral in the lower line of Eq. (24) is discretized by a time grid

$$\vec{\tau} = \{\tau_i\}_{i=1}^N \tag{29}$$

and integration weights

$$\vec{\sigma} = \{\sigma_i\}_{i=1}^N. \tag{30}$$

The corresponding error function reads

$$\hat{\eta}_{\vec{\sigma}, \vec{\tau}}(x) = \frac{1}{2x} - 2 \sum_{i=1}^N \sigma_i \hat{\phi}_{\tau_i}^2(x). \tag{31}$$

For both error functions, Eqs. (28) and (31), the transition energies are restricted to the interval

$$x \in I^* = [\epsilon_{\min}, \epsilon_{\max}], \tag{32}$$

$$\epsilon_{\min} := \min(\epsilon_a - \epsilon_j), \quad \epsilon_{\max} := \max(\epsilon_a - \epsilon_j), \tag{33}$$

where a, as before, refers to an unoccupied state, and j to an occupied state. The minimax grid parameters $\{\gamma_k^*, \omega_k^*\}_{k=1}^N$, $\{\sigma_i^*, \tau_i^*\}_{i=1}^N$ are defined as parameters that minimize the maximum norm of the error functions $\eta_{\vec{\gamma}, \vec{\omega}}(x)$ and $\hat{\eta}_{\vec{\sigma}, \vec{\tau}}(x)$,

$$\{\gamma_k^*, \omega_k^*\}_{k=1}^N := \arg\min_{\{\gamma_k, \omega_k\}_{k=1}^N} \max_{x \in I^*} |\eta_{\vec{\gamma}, \vec{\omega}}(x)|, \tag{34}$$

$$\{\sigma_i^*, \tau_i^*\}_{i=1}^N := \arg\min_{\{\sigma_i, \tau_i\}_{i=1}^N} \max_{x \in I^*} |\hat{\eta}_{\vec{\sigma}, \vec{\tau}}(x)|. \tag{35}$$

It is convenient to consider minimax time and frequency grids for the special interval [108,136]

$$x \in \tilde{I} := [1, R], \quad R := \frac{\epsilon_{\max}}{\epsilon_{\min}}. \tag{36}$$

The corresponding minimax grids $\{\tilde{\gamma}_k, \tilde{\omega}_k\}_{k=1}^N$ and $\{\tilde{\sigma}_i, \tilde{\tau}_i\}_{i=1}^N$ then only depend on N and R,

$$\{\tilde{\gamma}_k, \tilde{\omega}_k\}_{k=1}^N = \arg\min_{\{\gamma_k, \omega_k\}_{k=1}^N} \max_{x \in [1,R]} |\eta_{\vec{\gamma}, \vec{\omega}}(x)|, \tag{37}$$

$$\{\tilde{\sigma}_i, \tilde{\tau}_i\}_{i=1}^N = \arg\min_{\{\sigma_i, \tau_i\}_{i=1}^N} \max_{x \in [1,R]} |\hat{\eta}_{\vec{\sigma}, \vec{\tau}}(x)|. \tag{38}$$

The minimax grids $\{\gamma_k^*, \omega_k^*\}_{k=1}^N$, $\{\sigma_i^*, \tau_i^*\}_{i=1}^N$ for a specific molecule or material with interval $x \in I^* = [\epsilon_{\min}, \epsilon_{\max}]$ easily follow by rescaling [108,136],

$$\gamma_k^* = \frac{\tilde{\gamma}_k}{\epsilon_{\min}}, \quad \omega_k^* = \frac{\tilde{\omega}_k}{\epsilon_{\min}}, \tag{39}$$

$$\sigma_i^* = 2\epsilon_{\min}\tilde{\sigma}_i, \quad \tau_i^* = 2\epsilon_{\min}\tilde{\tau}_i. \tag{40}$$

According to the alternation theorem of Chebychev, there exists a reference set of $2N + 1$ extrema points such that the maximum error of the quadrature is minimized. This property is used in the sloppy Remez algorithm [137] to perform the minimizations in Eqs. (37) and (38) in practice [108].

D. Cosine and sine transformations

To convert between imaginary time and frequency grids [Eqs. (7), (10), and (12)], the functions $F(i\omega)$ and $\hat{F}(i\tau)$ are split into even and odd parts [110],

$$F(i\omega) = F^{\text{even}}(i\omega) + F^{\text{odd}}(i\omega), \tag{41}$$

$$\hat{F}(i\tau) = \hat{F}^{\text{even}}(i\tau) + \hat{F}^{\text{odd}}(i\tau), \tag{42}$$

with $F^{\text{even}}(x) = F^{\text{even}}(-x)$ and $F^{\text{odd}}(x) = -F^{\text{odd}}(-x)$. The corresponding nonuniform discrete Fourier transforms turn

into sine transforms and cosine transforms [110],

$$F^{\text{even}}(i\omega_k) = \sum_{j=1}^{N} \delta_{kj} \cos{(\omega_k \tau_j)} \hat{F}^{\text{even}}(i\tau_j), \qquad (43)$$

$$F^{\text{odd}}(i\omega_k) = i \sum_{j=1}^{N} \lambda_{kj} \sin{(\omega_k \tau_j)} \hat{F}^{\text{odd}}(i\tau_j), \qquad (44)$$

$$\hat{F}^{\text{even}}(i\tau_j) = \sum_{k=1}^{N} \eta_{jk} \cos{(\tau_j \omega_k)} F^{\text{even}}(i\omega_k), \qquad (45)$$

$$\hat{F}^{\text{odd}}(i\tau_j) = -i \sum_{k=1}^{N} \zeta_{jk} \sin{(\tau_j \omega_k)} F^{\text{odd}}(i\omega_k), \qquad (46)$$

where the time points τ_j and frequency points ω_k are precalculated from Eqs. (39) and (40). The Fourier weights $\delta_{kj}, \lambda_{kj}, \eta_{jk}, \zeta_{jk}$ are computed by least-squares minimization in the following way, exemplarily shown for δ_{kj} from Eq. (43): one inserts the auxiliary functions Eqs. (19) and (20) for $F^{\text{even}}(i\omega_k)$ and $\hat{F}^{\text{even}}(i\tau_j)$ so that the error function of Eq. (43) reads

$$\eta^c_{\overrightarrow{\delta^{(k)}}}(x) = \frac{2x}{x^2 + \omega_k^2} - \sum_{j=1}^{N} \delta_{kj} \cos{(\omega_k \tau_j)} e^{-x\tau_j}, \qquad (47)$$

where we abbreviate $\overrightarrow{\delta^{(k)}} := \{\delta_{kj}\}_{j=1}^{N}$. $\overrightarrow{\delta^{(k)}}$ is then computed by linear-least-squares minimization of $\eta^c_{\overrightarrow{\delta^{(k)}}}(x)$,

$$\overrightarrow{\delta^{(k)}} = ((\mathbf{X}^{(k)})^{\text{T}} \mathbf{X}^{(k)})^{-1} (\mathbf{X}^{(k)})^{\text{T}} \overrightarrow{y^{(k)}},$$

$$X_{\alpha j}^{(k)} = \cos{(\omega_k \tau_j)} e^{-x_\alpha \tau_j}, \qquad y_\alpha^{(k)} = \frac{2x_\alpha}{x_\alpha^2 + \omega_k^2}. \qquad (48)$$

We distribute the grid points $\{x_\alpha\}$ in the interval $[1, R]$ with a spacing that is equidistant on a logarithmic scale. We use $m = 200$ grid points in every interval $[1,10]$, $[10,100]$, etc., so that the total number of grid points x_α used is the closest integer to $m \log_{10}(R) + 1$.

E. A priori assessment of the precision of minimax grids

The challenge in generating minimax grids is that the sloppy Remez algorithm to minimize error functions (37) and (38) is ill conditioned and may sensitively depend on initial conditions [108]. In a nutshell, this is because the value of the error functions (28) and (31) can be as small as machine precision while terms appearing in Eqs. (28) and (31) are in the order of one. To address this challenge, we have used quadruple precision in our implementation of the sloppy Remez algorithm. Still, the sloppy Remez algorithm to generate minimax grids is numerically unstable and it frequently finds only local minima and not the global optimization minimum. In such cases, the minimax grid is not optimal for certain N and certain R. However, not fully optimal minimax grids can be sufficiently accurate for GW or RPA.

In Sec. V, we will describe detailed benchmarks for GW and RPA calculations. However, before this, the quality of the grids can already been assessed by testing exact properties of Fourier transforms. As a measure for the frequency integration error of the direct MP2 frequency integral in Eq. (21) and the RPA frequency integral in Eq. (1), we define the minimax
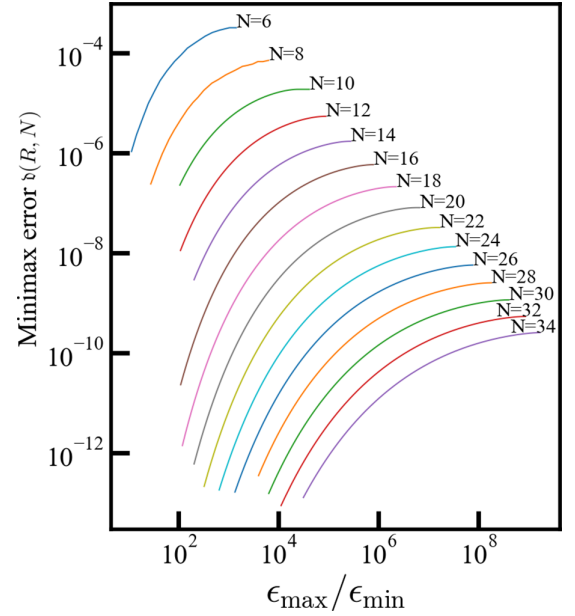

FIG. 1. Minimax error, Eq. (49), as a function of the energy range $R = \epsilon_{\max}/\epsilon_{\min}$ for minimax grids with varying number of integrations points N.

error

$$\mathfrak{d}(R, N) = \max_{x \in [1,R]} \left| \eta_{\{\tilde{\gamma}_k, \tilde{\omega}_k\}_{k=1}^{N}}(x) \right|. \qquad (49)$$

$\eta_{\{\tilde{\gamma}_k, \tilde{\omega}_k\}_{k=1}^{N}}(x)$ is the error of the frequency integration and is defined in Eq. (28). $\{\tilde{\gamma}_k, \tilde{\omega}_k\}_{k=1}^{N}$ is the minimax grid as computed from Eq. (37).

The minimax error $\mathfrak{d}(R, N)$ is plotted in Fig. 1 as a function of the number of grid points N and the energy range R. We observe that for a given system (molecule or solid) with fixed range R, the error decreases exponentially with increasing N. Conversely, increasing R by varying the system from small to large energy gaps leads to an increase in $\mathfrak{d}$. An upper range $R_c(N)$ exists, such that the minimax grid is identical for all $R > R_c(N)$ with saturating error, $\mathfrak{d}(R, N) = \mathfrak{d}(R_c(N), N)$ for $R > R_c(N)$ [109,138]. We thus only report minimax grids up to the upper range $R_c(N)$.

IV. COMPUTATIONAL DETAILS

A. Test systems

For molecules, benchmarks were performed for the Thiel [139] and GW100 [61] sets. The Thiel set consists of 28 small organic molecules composed of C, N, O, and H. The geometries were taken from Ref. [139]. The GW100 set contains small molecules with covalent and ionic bonds covering a wide range of the periodic table. The geometries were taken from Ref. [61]. For 2D semiconductors, four monolayer materials MoS_2, $MoSe_2$, WS_2, and WSe_2 were considered. The geometries were taken from the C2DB database [19]. For three-dimensional (3D) bulk crystals, the diamond structure of Si and C, zinc-blende structure of BN, GaAs, and SiC, and the rocksalt structure of MgO and LiF were selected. The lattice parameters were taken from Ref. [110]. The k-mesh settings given in Table I were used for all calculations. In the interest

TABLE I. Parameters for periodic conventional *GW* and low-scaling *GW* calculations when using ABINIT. E_c denotes the energy cutoff for expanding Bloch wavefunctions, E_c^ϵ the energy cutoff for the dielectric matrix and N_{bands} the number of bands for computing the Green's functions. All the k meshes are Γ centered.

	k mesh	E_c (Ha)	E_c^ϵ (Ha)	N_{bands}
Si	$4 \times 4 \times 4$	24	10	500
LiF	$8 \times 8 \times 8$	48	12	1000
SiC	$8 \times 8 \times 8$	48	12	1000
C	$6 \times 6 \times 6$	45	8	1000
BN	$4 \times 4 \times 4$	48	12	1000
MgO	$4 \times 4 \times 4$	50	12	1000
GaAs	$8 \times 8 \times 8$	48	12	1000

of open materials science data [140,141], we made the input and output files of all calculations available on the NOMAD repository [142].

B. FHI-aims

FHI-aims is an all-electron electronic structure code based on numerical atom-centered orbitals (NAOs) [127]. All canonical RPA calculations were performed with FHI-aims. The RPA implementations in FHI-aims scale $\mathcal{O}(N_{\text{at}}^4)$ with respect to system size N_{at} and are based on the resolution-of-the-identity (RI) approach, [143–146] refactoring the four-center electron repulsion integrals in a product of three- and two-center integrals. For finite systems, the RPA implementation [147] relies on a global RI scheme with a Coulomb metric (RI-V), while for extended systems a localized variant (RI-LVL) is employed [148,149].

Molecular RPA calculations were performed for the Thiel benchmark set using the cc-pVTZ Dunning basis set [150], which is an all-electron basis set of contracted spherical Gaussian orbitals. In FHI-aims, Gaussian basis sets are presented numerically to adhere to the NAO scheme. For the crystalline systems, we employed the hierarchical *tier 2* NAO basis functions [127]. For both, molecules and crystal, the RI auxiliary basis functions (ABFs) were autogenerated during runtime following the approach described in Ref. [147]. For the crystalline systems, we have added additional *4f* and *5g* functions to the autogenerated ABFs to increase the accuracy of the RI-LVL approach implemented for solids [149].

The RPA correlation energies were numerically computed on imaginary frequency grids [147]. We benchmarked three different grid types: the Gauss-Legendre (GL), modified Gauss-Legendre (mod-GL), and minimax quadrature grids. The standard and modified Gauss-Legendre quadratures are described in more detail in Appendix C of Ref. [147].

C. CP2K

CP2K is an electronic-structure code that employs Gaussian basis sets for expanding the KS orbitals [128]. CP2K can be used with Goedecker-Teter-Hutter pseudopotentials [151] (GTH) or as an all-electron code using the Gaussian and augmented plane-waves scheme (GAPW) [152]. CP2K features a low-scaling G_0W_0 implementation based on a

local-orbital-basis adaptation of the space-time method [107], where sparsity is introduced by combining a global RI scheme with a truncated Coulomb metric [24,113]. Low-scaling *GW* implementations for finite systems [113] and recently also for extended systems [24] are available.

We used the low-scaling G_0W_0 implementations in CP2K for performing the all-electron GW100 benchmark [61] and for computing the G_0W_0 bandgap of 2D materials with pseudopotentials. For the GW100 benchmark, we expanded molecular orbitals in the all-electron def2-QZVP [153] basis set and used def2-TZVPPD-RIFIT [154] as ABFs. For G_0W_0 benchmark calculations on 2D materials, we used 10×10 supercells, GTH pseudopotentials [151] with a TZV2P-MOLOPT basis set [155] and corresponding ABFs [24]. For molecules and 2D materials, we set a truncation radius of 3 Å [146,156] for the truncated Coulomb metric. Two- and three-center Coulomb integrals over Gaussian basis functions were computed with analytical schemes [157,158]. The self-energy was analytically continued from the imaginary to the real-frequency domain using a Padé model [61,159] with at most 16 parameters. Restricting the number of Padé parameters is motivated by the settings used in our GW100 reference data as detailed in Sec. V B. For grid sizes larger than 16 time/frequency points, we still perform all operations for the full grid, ensuring accurate $i\omega/i\tau$ transformations. When performing the analytic continuation, 16 equidistant imaginary frequency points and the corresponding $\Sigma(i\omega)$ are selected out of the larger set.

D. ABINIT

ABINIT is an electronic-structure code that relies on plane-waves for the representation of wavefunctions, density, and other space-dependent quantities, with pseudopotentials or projector-augmented waves [129,130]. We used ABINIT for the calculations of G_0W_0 band gaps of the crystalline systems with the specifications given in Table I and norm-conserving pseudopotentials [160] from the PseudoDojo project [161] (standard accuracy table and the recommended cutoff energy for the plane-wave expansion of the KS states). The conventional *GW* implementation in ABINIT scales with $O(N_{\text{at}}^4)$ and computes the RPA susceptibility along the imaginary frequency axis using the exact Adler-Wiser expression. For the conventional *GW* calculations, the self-energy was evaluated directly along the imaginary frequency axis using a linear mesh extending up to 50 eV and 60 points. The new cubic-scaling *GW* implementation is based on the space-time approach [107] and will be made available in ABINIT version 10. In the low-scaling *GW* calculations, we use minimax grids with 10, 20, and 30 points provided by the GreenX library [125]. The noninteracting susceptibility and the correlation part of the self-energy were computed using fast Fourier transforms in a supercell followed by a Padé-based analytic continuation of the matrix elements of the self-energy as discussed in Ref. [110]. In all conventional and low-scaling *GW* calculations, the number of imaginary frequencies used for the Padé was set to be equal to the number of frequency points used to sample the self-energy.

The integrable Coulomb singularity is treated by means of the auxiliary function proposed in Ref. [162] to accelerate
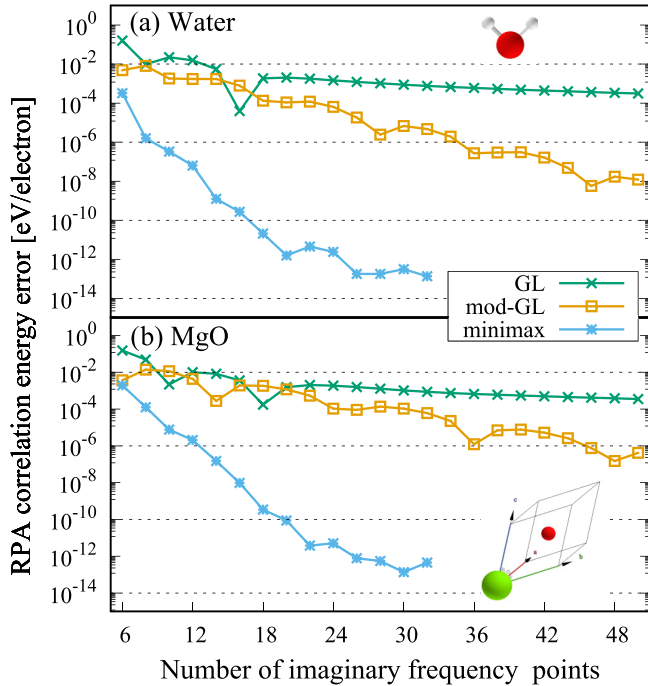
FIG. 2. Errors of the RPA correlation energy for the water molecule (top) and the MgO bulk (bottom) using the GL, mod-GL, and minimax imaginary frequency grids. The RPA error reported on the vertical axis employs as reference point the RPA energy calculated with the minimax grid containing 34 points. The error is given in eV/electron, dividing the absolute RPA correlation energy by the number of electrons per molecule or by the number of electrons in the unit cell.

the convergence with respect to Brillouin zone sampling. The calculation of the head and wings of the polarizability takes into account the nonlocal part of the KS Hamiltonian that arises from the pseudopotentials into account [163].

V. *GW* AND RPA BENCHMARK CALCULATIONS WITH MINIMAX GRIDS FROM GREENX

A. Conventional RPA for molecules and solids

While the primary purpose of the minimax grids is to facilitate low-scaling RPA and *GW* calculations, they can be also utilized to reduce the computational prefactor in conventional RPA implementations with $O(N_{\mathrm{at}}^4)$ complexity. We demonstrate this in Fig. 2 for a single water molecule (top) and bulk MgO (bottom). Figure 2 reports the error of the RPA correlation energies calculated with GL and mod-GL grids with 650 points and minimax grids with 632 points. The RPA energy obtained with the 34-point minimax grid is used as reference.

Figure 2 shows that the GL quadrature converges slowly, while the mod-GL grids exhibit a faster convergence as already discussed in Ref. [147]. The minimax grids display the fastest convergence. We set a target accuracy of 10^{-6} eV/electron, which is motivated by the size of the error introduced by the RI-V approach. RI-V is implemented in FHI-aims for finite RPA calculations and considered the most accurate RI scheme [146]. Recently, we showed for MP2
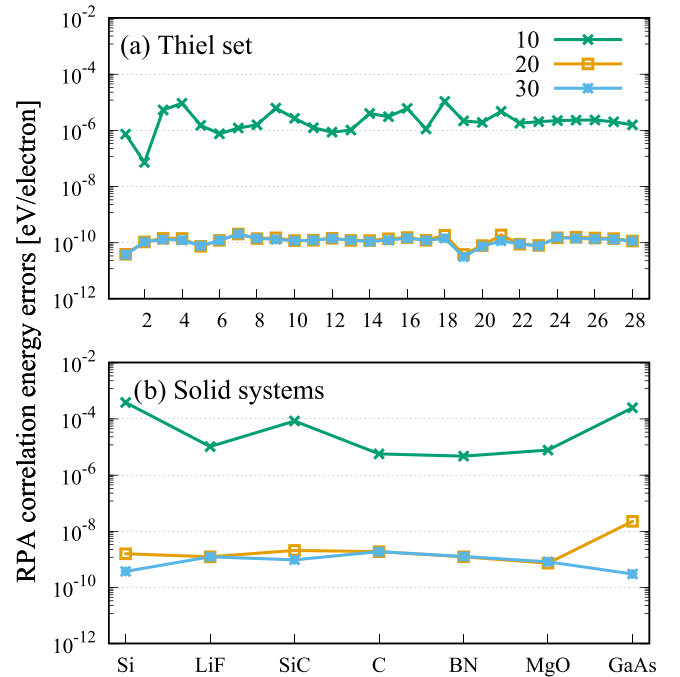

FIG. 3. Errors of the RPA correlation energy of (a) the Thiel set and (b) solids when using minimax frequency grids with 10, 20, and 30 grid points. The reference for computing the RPA error is the mod-GL grid with 200 frequency grid points. The error is given in eV/electron, dividing the absolute RPA correlation energy by the number of electrons per molecule or by the number of electrons in the unit cell.

correlation energies that RI-V introduces an average error of 5×10^{-6} eV/electron compared to RI-free results [164]. Similar RI errors are expected for RPA. The GL grids fail to achieve the desired accuracy for the grid sizes presented in Fig. 2. In contrast, the mod-GL grids surpass the accuracy threshold with over 36 and 46 frequency points for the water molecule and bulk MgO, respectively. With minimax grids, errors below 10^{-6} eV/electron are already achieved with 10 frequency points for water and 14 for MgO. Minimax frequency grids are therefore approximately 3.5-fold more efficient than mod-GL grids.

For even larger minimax grids of 20 points, the RPA integration errors drop below 10^{-10} eV/electron in both cases, as is evident in Fig. 2. The minimax error further decreases by two orders of magnitude to 10^{-12} eV/electron before leveling out at around 32 points. We found that it is not possible to converge the RPA correlation energies as tightly with the mod-GL grids, which eventually yield fluctuating errors around 10^{-9}–10^{-10} eV/electron. This is also the reason why we use the 34-point minimax grid as reference in Fig. 2 instead of a mod-GL grid with hundreds of points. The convergence behavior of the minimax grids for more than 20 grid points would not be adequately displayed.

Further benchmarks were performed with 10, 20, and 30 minimax grid points for molecules and crystalline systems as shown in Figs. 3(a) and 3(b). Taking the mod-GL result with 200 frequency points as our reference, we find that minimax grids with 10 points fail to converge all molecular and extended systems below the threshold of the RI-V

accuracy. However, we observe an excellent convergence for larger grids. All molecules from the Thiel set are converged within 10^{-9} eV/electron for minimax grids with 20 or more frequency points; see Fig. 3(a).

For solids shown in Fig. 3(b), we observe that the RPA correlation energy is converged to better than 10^{-8} eV/electron for 30 minimax frequency points. For 20 minimax points, the RPA correlation energy of GaAs still deviates by 2.2×10^{-8} eV/electron from the reference. This error is reduced by two orders of magnitudes for 30 minimax points instead. We note that even an error of 2.2×10^{-8} eV/electron is excellent when taking the RI-V error as target accuracy. Minimax grids with 20 grid points can therefore be considered a reliable choice for conventional RPA calculations. For completeness, the RPA data for the four systems (or set of systems), for the GL, modified GL and minimax cases, are gathered within the Supplemental Material [165] (Tables S1– S4).

B. Low-scaling *GW* for molecules

In this section, we present GW100 benchmark results for our minimax time and frequency grids employing the low-scaling G_0W_0 implementation in CP2K [113]. We computed quasiparticle energies of the highest occupied molecular orbitals (HOMOs) and lowest unoccupied molecular orbitals (LUMOs), for minimax grids with 10–32 points. We selected as our reference the G_0W_0@PBE results reported in Ref. [61], more precisely, the analytic continuation results from FHI-aims based on the Padé model 16 parameters and the def2-QZVP basis set. For the HOMOs, the five multi-solution cases were excluded, namely, BN, BeO, MgO, O_3, and CuCN.

Figure 4 summarizes the convergence of the G_0W_0@PBE HOMO and LUMO energies with respect to the number of minimax time and frequency points. We find that the mean absolute deviation (MAD) steadily decreases with the number of minimax points. Already for 24 minimax points, we observe an MAD smaller than 20 meV for both HOMOs and LUMOs. For grids with 28 points, the MAD drops below 10 meV. Figure 4 additionally reports the number of molecules with an absolute deviation (AD) below 10 meV and 20 meV. For 32 minimax points, 85 (out of 95) HOMO energies and 97 (out of 100) LUMO energies deviate by less than 10 meV from the reference value. Moreover, 92 HOMO and 100 LUMO energies are within the threshold of 20 meV.

For molecular benchmarks, our GW100 results are well within the target accuracy of a few meV we aim for when comparing different *GW* implementations using the same basis set. For example, the original GW100 benchmark study [61] reported a MAD of 3 meV and 6 meV for the HOMO and LUMO, respectively, comparing FHI-aims and RI-free Turbomole results at the def2-QZVP level. Furthermore, we conducted a similar convergence study as shown in Fig. 4 in our previous paper [113], where we also reported MADs below 10 meV for minimax grid sizes $\geqslant 28$ points.

C. Low-scaling *GW* for 2D materials

The unit cells of 2D materials can become large quickly, possibly requiring a hundred to thousands of atoms. An example are moiré structures formed from twisted transition
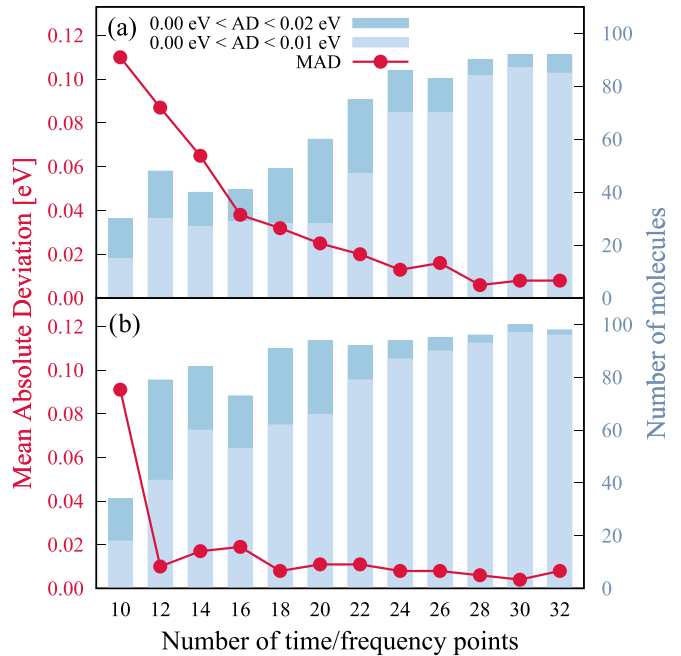

FIG. 4. GW100 benchmark of the G_0W_0@PBE energies computed with the low-scaling algorithm for (a) HOMOs and (b) LUMOs. The bars represent the number of molecules with a given absolute deviation from the FHI-aims values reported in Ref. [61]. The mean absolute deviation (MAD) as a function of number of time/frequency points is given by the red dots. Table S5 within the Supplemental Material [165] reports the raw data.

metal dichalcogenide (TMDC) bilayers [166–168]. The development of low-scaling algorithms is a promising strategy to make *GW* calculations for these systems computationally feasible [24]. Localized-basis-set frameworks are here particularly advantageous due to the large vacuum regions, which need to be added below and above the 2D slabs [18]. Such vacuum regions drastically increase the computational cost for plane-wave implementations, but not for localized-basis-functions schemes.

In this section, we present G_0W_0@LDA bandgap calculations for monolayer MoS_2, $MoSe_2$, WS_2, and WSe_2, which have previously been used as building blocks for TMDC-based Moiré structures [167,168]. Figure 5 reports the band gaps computed with 10, 20, and 30 time and frequency points using the recently developed periodic, low-scaling *GW* implementation in CP2K [24]. We find that the G_0W_0@LDA band gap changes on average by 20 meV and when increasing the minimax mesh size from 10 to 20 points and by 4 meV from 20 to 30 points. These findings indicate that a grid size of 20 is a reliable choice for the 2D case.

We report absolute gaps in Fig. 5 since reliable reference data for 2D materials are generally difficult to find [2]. Qiu *et al.* [18] showed that a very fine *k*-grid sampling is required for TMDC monolayers ($24 \times 24 \times 1$ grids). Equivalently, our recent study [24] demonstrated a slow convergence with the supercell size, necessitating supercell sizes of at least $10 \times 10 \times 1$. Due to these challenges, a benchmark set for highly accurate *GW* band structures of 2D monolayers has not been established yet to the best of our knowledge. In previous
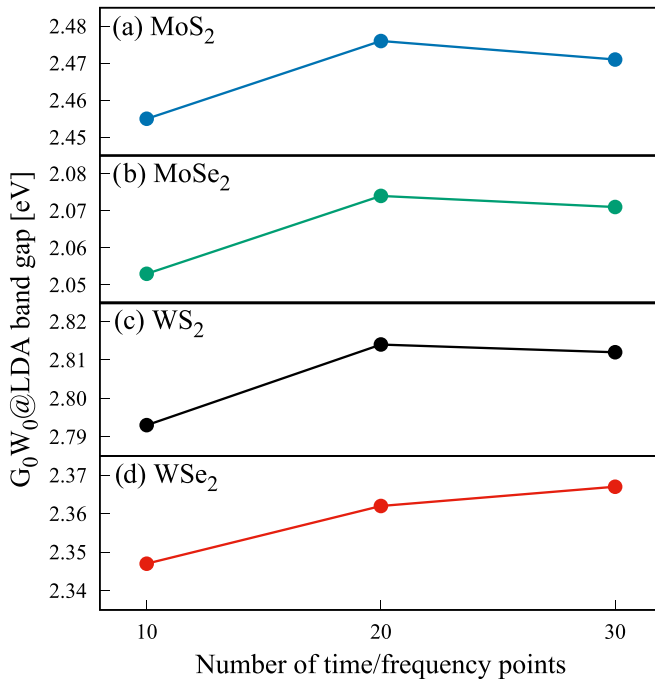
FIG. 5. G_0W_0@LDA bandgap of monolayer semiconductors computed with CP2K [24,128] as function of the number of points of the minimax time-frequency grid. Table S6 within the Supplemental Material [165] reports the raw data.

paper [24], well-converged G_0W_0@LDA gaps were collected from several codes [20,24,169] for the MoS_2, $MoSe_2$, WS_2, and WSe_2 monolayers, observing an average deviation of 55 meV between the codes. The accuracy of a minimax time-frequency grid with 10 points is already better than the difference between different *GW* codes.

D. Low-scaling *GW* for solids

As a preliminary accuracy check of the minimax grids, we have compared selected matrix elements of the susceptibility in Fourier space computed along the imaginary axis for conventional and low-scaling *GW* implementations (see Fig. S1 within the Supplemental Material [165]). The agreement between the two implementations is excellent. Small differences only arise for Fourier components of the imaginary part (see middle-right panel of Fig. S1 within the Supplemental Material [165]) but this is essentially numerical noise that does not affect our final results.

We then computed the direct band gaps of the seven solids introduced in Sec. IV A with the low-scaling *GW* implementation in ABINIT and then compared with the analogous results obtained with the conventional quartic-scaling *GW* implementation. The results obtained with the settings given in Table I are summarized in Fig. 6. As becomes clear from Fig. 6, the band gaps of the low-scaling implementation approach those of the conventional one with increasing number of frequency points. For 20 minimax points the difference is already below 10 meV. Our results are in line with a previous comparison for these materials. Liu *et al.* [110] also found a difference of 10 meV between their low-scaling and the conventional quartic-scaling *GW* implementation [170] in the
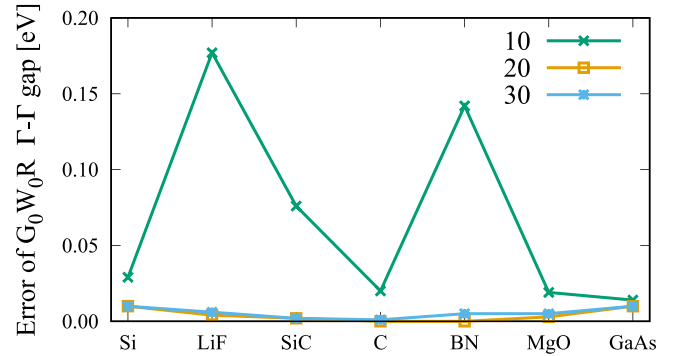

FIG. 6. The low-scaling *GW* error with respect to the conventional *GW* using ABINIT (See Table S7 within the Supplemental Material [165] for the raw data).

VASP code, using 20 minimax grid points in their space-time-based low-scaling implementation.

VI. CONCLUSIONS

The time-frequency component of the GreenX library [126], which provides minimax time-frequency grids along with corresponding quadrature weights to compute correlation energies and quasiparticle energies and weights for Fourier transforms, has recently been released. In the present paper, we linked the GreenX library to three codes (FHI-aims, CP2K, and ABINIT), and performed conventional RPA and low-scaling *GW* calculations for a variety of systems. Our test systems include the molecules of the Thiel and GW100 benchmark sets, four two-dimensional semiconductors (TMDC monolayer materials) and seven 3D bulk crystals. We found that the conventional RPA calculations are well converged within $< 10^{-7}$ eV/electron for minimax grids with 20 points, reducing the computational prefactor by a factor of ≈ 3 compared to calculations with conventional modified Gauss-Legendre grids. The RPA integration errors decrease to $< 10^{-8}$ eV/electron for even larger grids with 30 points. Low-scaling *GW* quasiparticle energies are converged to $\leqslant 10$ meV for all systems using only 30 minimax points. In most cases this excellent accuracy is already reached with 20 minimax grid points.

Our findings show that the time-frequency component of GreenX provides a reliable foundation for the development of low-scaling RPA and *GW* algorithms based on the space-time method. We also showed that minimax frequency grids can accelerate conventional RPA calculations. We plan on releasing other GreenX components, e.g., for the analytic continuation in the near future.

ACKNOWLEDGMENTS

[1] L. Hedin, New method for calculating the one-particle Green's function with application to the electron-gas problem, Phys. Rev. **139**, A796 (1965).

[2] D. Golze, M. Dvorak, and P. Rinke, The *GW* compendium: A practical guide to theoretical photoemission spectroscopy, Front. Chem. **7**, 377 (2019).

[3] L. Reining, The *GW* approximation: content, successes and limitations, WIREs Comput. Mol. Sci. **8**, e1344 (2018).

[4] M. Stankovski, G. Antonius, D. Waroquiers, A. Miglio, H. Dixit, K. Sankaran, M. Giantomassi, X. Gonze, M. Côté, and G.-M. Rignanese, G^0W^0 band gap of ZnO: Effects of plasmon-pole models, Phys. Rev. B **84**, 241201(R) (2011).

[5] J.-L. Li, G.-M. Rignanese, and S. G. Louie, Quasiparticle energy bands of NiO in the *GW* approximation, Phys. Rev. B **71**, 193102 (2005).

[6] F. Bruneval and X. Gonze, Accurate *GW* self-energies in a plane-wave basis using only a few empty states: Towards large systems, Phys. Rev. B **78**, 085125 (2008).

[7] D. Nabok, A. Gulans, and C. Draxl, Accurate all-electron G_0W_0 quasiparticle energies employing the full-potential augmented plane-wave method, Phys. Rev. B **94**, 035118 (2016).

[8] T. Aoki and K. Ohno, Accurate quasiparticle calculation of x-ray photoelectron spectra of solids, J. Phys.: Condens. Matter **30**, 21LT01 (2018).

[9] D. Golze, J. Wilhelm, M. J. van Setten, and P. Rinke, Core-level binding energies from *GW*: An efficient full-frequency approach within a localized basis, J. Chem. Theory Comput. **14**, 4856 (2018).

[10] D. Golze, L. Keller, and P. Rinke, Accurate absolute and relative core-level binding energies from *GW*, J. Phys. Chem. Lett. **11**, 1840 (2020).

[11] L. Keller, V. Blum, P. Rinke, and D. Golze, Relativistic correction scheme for core-level binding energies from *GW*, J. Chem. Phys. **153**, 114110 (2020).

[12] T. Zhu and G. K.-L. Chan, All-electron Gaussian-based G_0W_0 for valence and core excitation energies of periodic systems, J. Chem. Theory Comput. **17**, 727 (2021).

[13] D. Mejia-Rodriguez, A. Kunitsa, E. Aprà, and N. Govind, Scalable molecular *GW* calculations: Valence and core spectra, J. Chem. Theory Comput. **17**, 7504 (2021).

[14] D. Mejia-Rodriguez, A. Kunitsa, E. Aprà, and N. Govind, Basis set selection for molecular core-level *GW* calculations, J. Chem. Theory Comput. **18**, 4919 (2022).

[15] J. Li, Y. Jin, P. Rinke, W. Yang, and D. Golze, Benchmark of *GW* methods for core-level binding energies, J. Chem. Theory Comput. **18**, 7570 (2022).

[16] R. L. Panadés-Barrueta and D. Golze, Accelerating core-level *GW* calculations by combining the contour deformation approach with the analytic continuation of *W*, J. Chem. Theory Comput. **19**, 5450 (2023).

[17] A. Molina-Sánchez, D. Sangalli, K. Hummer, A. Marini, and L. Wirtz, Effect of spin-orbit interaction on the optical spectra of single-layer, double-layer, and bulk MoS_2, Phys. Rev. B **88**, 045412 (2013).

[18] D. Y. Qiu, F. H. da Jornada, and S. G. Louie, Screening and many-body effects in two-dimensional crystals: Monolayer MoS_2, Phys. Rev. B **93**, 235435 (2016).

[19] M. N. Gjerding, A. Taghizadeh, A. Rasmussen, S. Ali, F. Bertoldo, T. Deilmann, N. R. Knøsgaard, M. Kruse, A. H. Larsen, S. Manti *et al.*, Recent progress of the Computational 2D Materials Database (C2DB), 2D Mater. **8**, 044002 (2021).

[20] A. Rasmussen, T. Deilmann, and K. S. Thygesen, Towards fully automated *GW* band structure calculations: What we can learn from 60.000 self-energy evaluations, npj Comput. Mater. **7**, 22 (2021).

[21] E. Mitterreiter, B. Schuler, A. Micevic, D. Hernangómez-Pérez, K. Barthelmi, K. A. Cochrane, J. Kiemle, F. Sigger, J. Klein, E. Wong *et al.*, The role of chalcogen vacancies for atomic defect emission in MoS_2, Nat. Commun. **12**, 3822 (2021).

[22] K.-Q. Lin, C. S. Ong, S. Bange, P. E. Faria Junior, B. Peng, J. D. Ziegler, J. Zipfel, C. Bäuml, N. Paradiso, K. Watanabe *et al.*, Narrow-band high-lying excitons with negative-mass electrons in monolayer WSe_2, Nat. Commun. **12**, 5500 (2021).

[23] A. Guandalini, P. D'Amico, A. Ferretti, and D. Varsano, Efficient *GW* calculations in two dimensional materials through a stochastic integration of the screened potential, npj Comput. Mater. **9**, 44 (2023).

[24] M. Graml, K. Zollner, D. Hernangómez-Pérez, P. E. Faria Junior, and J. Wilhelm, Low-scaling *GW* algorithm applied to twisted transition-metal dichalcogenide heterobilayers, J. Chem. Theory Comput. (2024).

[25] M. R. Filip, G. E. Eperon, H. J. Snaith, and F. Giustino, Steric engineering of metal-halide perovskites with tunable optical band gaps, Nat. Commun. **5**, 5757 (2014).

[26] Y. Cho and T. C. Berkelbach, Optical properties of layered hybrid organic–inorganic halide perovskites: A tight-binding GW-BSE study, J. Phys. Chem. Lett. **10**, 6189 (2019).

[27] R.-I. Biega, Y. Chen, M. R. Filip, and L. Leppert, Chemical mapping of excitons in halide double perovskites, Nano Lett. **23**, 8155 (2023).

[28] J. McArthur, M. R. Filip, and D. Y. Qiu, Minimal molecular building blocks for screening in quasi-two-dimensional organic–inorganic lead halide perovskites, Nano Lett. **23**, 3796 (2023).

[29] G. Biffi, Y. Cho, R. Krahne, and T. C. Berkelbach, Excitons and their fine structure in lead halide perovskite nanocrystals from atomistic GW/BSE calculations, J. Phys. Chem. C **127**, 1891 (2023).

[30] L. Leppert, Excitons in metal-halide perovskites from first-principles many-body perturbation theory, J. Chem. Phys. **160**, 050902 (2024).

[31] O. Çaylak and B. Baumeier, Excited-state geometry optimization of small molecules with many-body Green's functions theory, J. Chem. Theory Comput. **17**, 879 (2021).

[32] J. A. Berger, P.-F. Loos, and P. Romaniello, Potential energy surfaces without unphysical discontinuities: The Coulomb hole plus screened exchange approach, J. Chem. Theory Comput. **17**, 191 (2021).

[33] I. Knysh, K. Letellier, I. Duchemin, X. Blase, and D. Jacquemin, Excited state potential energy surfaces of *N*-phenylpyrrole upon twisting: Reference values and comparison between BSE/*GW* and TD-DFT, Phys. Chem. Chem. Phys. **25**, 8376 (2023).

[34] C. Holzer, A. M. Teale, F. Hampe, S. Stopkowicz, T. Helgaker, and W. Klopper, *GW* quasiparticle energies of atoms in strong magnetic fields, J. Chem. Phys. **150**, 214112 (2019).

[35] Y. J. Franzke, C. Holzer, and F. Mack, NMR coupling constants based on the Bethe-Salpeter equation in the *GW* approximation, J. Chem. Theory Comput. **18**, 1030 (2022).

[36] C. Holzer, Practical Post-KohnSham methods for time-reversal symmetry breaking references, J. Chem. Theory Comput. **19**, 3131 (2023).

[37] M. Kühn and F. Weigend, One-electron energies from the two-component *GW* method, J. Chem. Theory Comput. **11**, 969 (2015).

[38] C. Holzer and W. Klopper, Ionized, electron-attached, and excited states of molecular systems with spin orbit coupling: Two-component *GW* and Bethe-Salpeter implementations, J. Chem. Phys. **150**, 204116 (2019).

[39] A. Förster, E. van Lenthe, E. Spadetto, and L. Visscher, Two-component *GW* calculations: Cubic scaling implementation and comparison of vertex-corrected and partially self-consistent *GW* variants, J. Chem. Theory Comput. **19**, 5958 (2023).

[40] M. Kehry, W. Klopper, and C. Holzer, Robust relativistic many-body Green's function based approaches for assessing core ionized and excited states, J. Chem. Phys. **159**, 044116 (2023).

[41] A. Stuke, C. Kunkel, D. Golze, M. Todorović, J. T. Margraf, K. Reuter, P. Rinke, and H. Oberhofer, Atomic structures and orbital energies of 61,489 crystal-forming organic molecules, Sci. Data **7**, 58 (2020).

[42] J. Westermayr and R. J. Maurer, Physically inspired deep learning of molecular excitations and photoemission spectra, Chem. Sci. **12**, 10755 (2021).

[43] D. Golze, M. Hirvensalo, P. Hernández-León, A. Aarva, J. Etula, T. Susi, P. Rinke, T. Laurila, and M. A. Caro, Accurate computational prediction of core-electron binding energies in carbon-based materials: A machine-learning model combining density-functional theory and *GW*, Chem. Mater. **34**, 6240 (2022).

[44] A. Fediai, P. Reiser, J. E. O. Peña, W. Wenzel, and P. Friedrich, Interpretable delta-learning of *GW* quasiparticle energies from GGA-DFT, Mach. Learn.: Sci. Technol. **4**, 035045 (2023).

[45] B. Mondal, J. Westermayr, and R. Tonner-Zech, Machine learning for accelerated bandgap prediction in strain-engineered quaternary III–V semiconductors, J. Chem. Phys. **159**, 104702 (2023).

[46] M. G. Zauchner, A. Horsfield, and J. Lischner, Accelerating *GW* calculations through machine-learned dielectric matrices, npj Comput. Mater. **9**, 184 (2023).

[47] C. Venturella, C. Hillenbrand, J. Li, and T. Zhu, Machine learning many-body Green's functions for molecular excitation spectra, J. Chem. Theory Comput. **20**, 143 (2024).

[48] C. Attaccalite, M. Grüning, and A. Marini, Real-time approach to the optical properties of solids and nanostructures: Time-dependent Bethe-Salpeter equation, Phys. Rev. B **84**, 245110 (2011).

[49] X. Jiang, Q. Zheng, Z. Lan, W. A. Saidi, X. Ren, and J. Zhao, Real-time *GW*-BSE investigations on spin-valley exciton dynamics in monolayer transition metal dichalcogenide, Sci. Adv. **7**, eabf3759 (2021).

[50] Y.-H. Chan, D. Y. Qiu, F. H. da Jornada, and S. G. Louie, Giant exciton-enhanced shift currents and direct current conduction with subbandgap photo excitations produced by many-electron interactions, Proc. Natl. Acad. Sci. USA **118**, e1906938118 (2021).

[51] N. Schlünzen, J.-P. Joost, and M. Bonitz, Achieving the scaling limit for nonequilibrium Green functions simulations, Phys. Rev. Lett. **124**, 076601 (2020).

[52] E. Perfetto, Y. Pavlyukh, and G. Stefanucci, Real-Time *GW*: Toward an *ab initio* description of the ultrafast carrier and exciton dynamics in two-dimensional materials, Phys. Rev. Lett. **128**, 016801 (2022).

[53] R. Tuovinen, D. Golež, M. Eckstein, and M. A. Sentef, Comparing the generalized Kadanoff-Baym ansatz with the full Kadanoff-Baym equations for an excitonic insulator out of equilibrium, Phys. Rev. B **102**, 115157 (2020).

[54] R. Tuovinen, R. van Leeuwen, E. Perfetto, and G. Stefanucci, Electronic transport in molecular junctions: The generalized Kadanoff–Baym ansatz with initial contact and correlations, J. Chem. Phys. **154**, 094104 (2021).

[55] R. Tuovinen, Y. Pavlyukh, E. Perfetto, and G. Stefanucci, Time-linear quantum transport simulations with correlated nonequilibrium Green's functions, Phys. Rev. Lett. **130**, 246301 (2023).

[56] Y. Pavlyukh, R. Tuovinen, E. Perfetto, and G. Stefanucci, Cheers: A linear-scaling KBE+GKBA code, Phys. Status Solidi B, 2300504 (2023).

[57] F. Bruneval, N. Dattani, and M. J. van Setten, The *GW* miracle in many-body perturbation theory for the ionization potential of molecules, Front. Chem. **9**, 749779 (2021).

[58] R. Orlando, P. Romaniello, and P.-F. Loos, The three channels of many-body perturbation theory: *GW*, particle-particle, and electron-hole *T*-matrix self-energies, J. Chem. Phys. **159**, 184113 (2023).

[59] S. Marek and R. Korytár, Widening of the fundamental gap in cluster *GW* for metal-molecular interfaces, Phys. Chem. Chem. Phys. **26**, 2127 (2024).

[60] A. Ammar, A. Marie, M. Rodríguez-Mayorga, H. G. A. Burton, and P.-F. Loos, Can *GW* handle multireference systems? J. Chem. Phys. **160**, 114101 (2024).

[61] M. J. van Setten, F. Caruso, S. Sharifzadeh, X. Ren, M. Scheffler, F. Liu, J. Lischner, L. Lin, J. R. Deslippe, S. G. Louie, C. Yang, F. Weigend, J. B. Neaton, F. Evers, and P. Rinke, *GW100:* Benchmarking G_0W_0 for molecular systems, J. Chem. Theory Comput. **11**, 5665 (2015).

[62] E. Maggio, P. Liu, M. J. van Setten, and G. Kresse, *GW100:* A plane wave perspective for small molecules, J. Chem. Theory Comput. **13**, 635 (2017).

[63] M. J. van Setten, M. Giantomassi, X. Gonze, G.-M. Rignanese, and G. Hautier, Automation methodologies and large-scale validation for *GW*: Towards high-throughput *GW* calculations, Phys. Rev. B **96**, 155207 (2017).

[64] W. Gao and J. R. Chelikowsky, Real-space based benchmark of G_0W_0 calculations on GW100: Effects of semicore orbitals and orbital reordering, J. Chem. Theory Comput. **15**, 5299 (2019).

[65] M. Govoni and G. Galli, GW100: Comparison of methods and accuracy of results obtained with the WEST code, J. Chem. Theory Comput. **14**, 1895 (2018).

[66] A. Förster and L. Visscher, GW100: A Slater-type orbital perspective, J. Chem. Theory Comput. **17**, 5080 (2021).

[67] T. Rangel, M. Del Ben, D. Varsano, G. Antonius, F. Bruneval, F. H. da Jornada, M. J. van Setten, O. K. Orhan, D. D. ORegan, A. Canning *et al.*, Reproducibility in G_0W_0 calculations for solids, Comput. Phys. Commun. **255**, 107242 (2020).

[68] D. Bohm and D. Pines, A collective description of electron interactions: III. Coulomb interactions in a degenerate electron gas, Phys. Rev. **92**, 609 (1953).

[69] M. Gell-Mann and K. A. Brueckner, Correlation energy of an electron gas at high density, Phys. Rev. **106**, 364 (1957).

[70] W. Kohn and L. J. Sham, Self-consistent equations including exchange and correlation effects, Phys. Rev. **140**, A1133 (1965).

[71] J. P. Perdew, K. Burke, and M. Ernzerhof, Generalized gradient approximation made simple, Phys. Rev. Lett. **77**, 3865 (1996).

[72] C. Adamo and V. Barone, Toward reliable density functional methods without adjustable parameters: The PBE0 model, J. Chem. Phys. **110**, 6158 (1999).

[73] H. Eshuis, J. E. Bates, and F. Furche, Electron correlation methods based on the random phase approximation, Theor. Chem. Acc. **131**, 1084 (2012).

[74] X. Ren, P. Rinke, C. Joas, and M. Scheffler, Random-phase approximation and its applications in computational chemistry and materials science, J. Mater. Sci. **47**, 7447 (2012).

[75] J. Harl, L. Schimka, and G. Kresse, Assessing the quality of the random phase approximation for lattice constants and atomization energies of solids, Phys. Rev. B **81**, 115126 (2010).

[76] F. Furche, Molecular tests of the random phase approximation to the exchange-correlation energy functional, Phys. Rev. B **64**, 195120 (2001).

[77] M. Fuchs and X. Gonze, Accurate density functionals: Approaches using the adiabatic-connection fluctuation-dissipation theorem, Phys. Rev. B **65**, 235109 (2002).

[78] G. E. Scuseria, T. M. Henderson, and D. C. Sorensen, The ground state correlation energy of the random phase approximation from a ring coupled cluster doubles approach, J. Chem. Phys. **129**, 231101 (2008).

[79] E. Spadetto, P. H. T. Philipsen, A. Forster, and L. Visscher, Toward pair atomic density fitting for correlation energies with benchmark accuracy, J. Chem. Theory Comput. **19**, 1499 (2023).

[80] A. M. Burow, J. E. Bates, F. Furche, and H. Eshuis, Analytical first-order molecular properties and forces within the adiabatic connection random phase approximation, J. Chem. Theory Comput. **10**, 180 (2014).

[81] B. Ramberger, T. Schäfer, and G. Kresse, Analytic interatomic forces in the random phase approximation, Phys. Rev. Lett. **118**, 106403 (2017).

[82] M. N. Tahir, T. Zhu, H. Shang, J. Li, V. Blum, and X. Ren, Localized resolution of identity approach to the analytical gradients of random-phase approximation ground-state energy: Algorithm and benchmarks, J. Chem. Theory Comput. **18**, 5297 (2022).

[83] V. Drontschenko, D. Graf, H. Laqua, and C. Ochsenfeld, Efficient method for the computation of frozen-core nuclear gradients within the random phase approximation, J. Chem. Theory Comput. **18**, 7359 (2022).

[84] A. Bussy, O. Schütt, and J. Hutter, Sparse tensor based nuclear gradients for periodic Hartree–Fock and low-scaling correlated wave function methods in the CP2K software package: A massively parallel and GPU accelerated implementation, J. Chem. Phys. **158**, 164109 (2023).

[85] F. Stein and J. Hutter, Massively parallel implementation of gradients within the random phase approximation: Application to the polymorphs of benzene, J. Chem. Phys. **160**, 024120 (2024).

[86] P. Liu, C. Verdi, F. Karsai, and G. Kresse, Phase transitions of zirconia: Machine-learned force fields beyond density functional theory, Phys. Rev. B **105**, L060102 (2022).

[87] S. Riemelmoser, C. Verdi, M. Kaltak, and G. Kresse, Machine learning density functionals from the random-phase approximation, J. Chem. Theory Comput. **19**, 7287 (2023).

[88] P. Liu, J. Wang, N. Avargues, C. Verdi, A. Singraber, F. Karsai, X.-Q. Chen, and G. Kresse, Combining machine learning and many-body calculations: Coverage-dependent adsorption of CO on Rh(111), Phys. Rev. Lett. **130**, 078001 (2023).

[89] M. Hellgren, D. Contant, T. Pitts, and M. Casula, High-pressure II-III phase transition in solid hydrogen: Insights from state-of-the-art *ab initio* calculations, Phys. Rev. Res. **4**, L042009 (2022).

[90] T. Braeckevelt, R. Goeminne, S. Vandenhaute, S. Borgmans, T. Verstraelen, J. A. Steele, M. B. J. Roeffaers, J. Hofkens, S. M. J. Rogge, and V. Van Speybroeck, Accurately determining the phase transition temperature of $CsPbI_3$ via random-phase approximation calculations and phase-transferable machine learning potentials, Chem. Mater. **34**, 8561 (2022).

[91] A. Hellier, C. Chizallet, and P. Raybaud, $PtO_xCl_y(OH)_z(H_2O)_n$ complexes under oxidative and reductive conditions: Impact of the level of theory on thermodynamic stabilities, ChemPhysChem **24**, e202200711 (2023).

[92] D. Dhingra, A. Shori, and A. Förster, Chemically accurate singlet-triplet gaps of organic chromophores and linear acenes by the random phase approximation and σ-functionals, J. Chem. Phys. **159**, 194105 (2023).

[93] R. Tyagi, A. Zen, and V. K. Voora, Quantifying the impact of halogenation on intermolecular interactions and binding modes of aromatic molecules, J. Phys. Chem. A **127**, 5823 (2023).

[94] J. Wilhelm, M. Del Ben, and J. Hutter, *GW* in the Gaussian and plane waves scheme with application to linear acenes, J. Chem. Theory Comput. **12**, 3623 (2016).

[95] M. Govoni and G. Galli, Large scale *GW* calculations, J. Chem. Theory Comput. **11**, 2680 (2015).

[96] M. Kim, S. Mandal, E. Mikida, K. Chandrasekar, E. Bohm, N. Jain, Q. Li, R. Kanakagiri, G. J. Martyna, L. Kale, and S. Ismail-Beigi, Scalable *GW* software for quasiparticle properties using OpenAtom, Comput. Phys. Commun. **244**, 427 (2019).

[97] D. Sangalli, A. Ferretti, H. Miranda, C. Attaccalite, I. Marri, E. Cannuccia, P. Melo, M. Marsili, F. Paleari, A. Marrazzo *et al.*, Many-body perturbation theory calculations using the yambo code, J. Phys.: Condens. Matter **31**, 325902 (2019).

[98] M. Del Ben, H. Felipe, A. Canning, N. Wichmann, K. Raman, R. Sasanka, C. Yang, S. G. Louie, and J. Deslippe, Large-scale *GW* calculations on pre-exascale HPC systems, Comput. Phys. Commun. **235**, 187 (2019).

[99] M. D. Ben, C. Yang, Z. Li, F. H. d. Jornada, S. G. Louie, and J. Deslippe, Accelerating large-scale excited-state *GW* calculations on leadership HPC systems, in *SC20: International Conference for High Performance Computing, Networking, Storage and Analysis* (IEEE, 2020), pp. 1–11.

[100] V. W.-z. Yu and M. Govoni, GPU acceleration of large-scale full-frequency *GW* calculations, J. Chem. Theory Comput. **18**, 4690 (2022).

[101] C.-N. Yeh, S. Iskakov, D. Zgid, and E. Gull, Fully self-consistent finite-temperature *GW* in Gaussian Bloch orbitals for solids, Phys. Rev. B **106**, 235104 (2022).

[102] I. Duchemin, D. Jacquemin, and X. Blase, Combining the *GW* formalism with the polarizable continuum model: A state-specific non-equilibrium approach, J. Chem. Phys. **144**, 164106 (2016).

[103] J. Li, G. D'Avino, I. Duchemin, D. Beljonne, and X. Blase, Combining the many-body *GW* formalism with classical polarizable models: Insights on the electronic structure of molecular solids, J. Phys. Chem. Lett. **7**, 2814 (2016).

[104] J. Li, G. D'Avino, I. Duchemin, D. Beljonne, and X. Blase, Accurate description of charged excitations in molecular solids from embedded many-body perturbation theory, Phys. Rev. B **97**, 035108 (2018).

[105] J. Tölle, T. Deilmann, M. Rohlfing, and J. Neugebauer, Subsystem-based *GW*/Bethe–Salpeter equation, J. Chem. Theory Comput. **17**, 2186 (2021).

[106] D. Amblard, X. Blase, and I. Duchemin, Many-body *GW* calculations with very large scale polarizable environments made affordable: A fully *ab-initio* QM/QM approach, J. Chem. Phys. **159**, 164107 (2023).

[107] H. N. Rojas, R. W. Godby, and R. J. Needs, Space-time method for *ab initio* calculations of self-energies and dielectric response functions of solids, Phys. Rev. Lett. **74**, 1827 (1995).

[108] M. Kaltak, J. Klimes, and G. Kresse, Low scaling algorithms for the random phase approximation: Imaginary time and Laplace transformations, J. Chem. Theory Comput. **10**, 2498 (2014).

[109] M. Kaltak, J. Klimeš, and G. Kresse, Cubic scaling algorithm for the random phase approximation: Self-interstitials and vacancies in Si, Phys. Rev. B **90**, 054115 (2014).

[110] P. Liu, M. Kaltak, J. Klimeš, and G. Kresse, Cubic scaling *GW*: Towards fast quasiparticle calculations, Phys. Rev. B **94**, 165109 (2016).

[111] C.-N. Yeh and M. A. Morales, Low-Scaling algorithms for *GW* and constrained random phase approximation using symmetry-adapted interpolative separable density fitting, arXiv:2401.12308.

[112] J. Wilhelm, D. Golze, L. Talirz, J. Hutter, and C. A. Pignedoli, Toward *GW* calculations on thousands of atoms, J. Phys. Chem. Lett. **9**, 306 (2018).

[113] J. Wilhelm, P. Seewald, and D. Golze, Low-scaling *GW* with benchmark accuracy and application to phosphorene nanosheets, J. Chem. Theory Comput. **17**, 1662 (2021).

[114] I. Duchemin and X. Blase, Cubic-scaling all-electron *GW* calculations with a separable density-fitting space-time approach, J. Chem. Theory Comput. **17**, 2383 (2021).

[115] A. Förster and L. Visscher, Low-order scaling G_0W_0 by pair atomic density fitting, J. Chem. Theory Comput. **16**, 7381 (2020).

[116] A. Förster and L. Visscher, Low-order scaling quasiparticle self-consistent *GW* for molecules, Front. Chem. **9**, 736591 (2021).

[117] A. Förster and L. Visscher, Quasiparticle self-consistent *GW*-Bethe-Salpeter equation calculations for large chromophoric systems, J. Chem. Theory Comput. **18**, 6779 (2022).

[118] J. Wilhelm, P. Seewald, M. Del Ben, and J. Hutter, Large-scale cubic-scaling random phase approximation correlation energy calculations using a Gaussian basis, J. Chem. Theory Comput. **12**, 5851 (2016).

[119] D. Graf, M. Beuerle, H. F. Schurkus, A. Luenser, G. Savasci, and C. Ochsenfeld, Accurate and efficient parallel implementation of an effective linear-scaling direct random phase approximation method, J. Chem. Theory Comput. **14**, 2505 (2018).

[120] M. Häser and J. Almlöf, Laplace transform techniques in Møller–Plesset perturbation theory, J. Chem. Phys. **96**, 489 (1992).

[121] D. Kats, D. Usvyat, S. Loibl, T. Merz, and M. Schütz, Comment on "Minimax approximation for the decomposition of energy denominators in Laplace-transformed Møller–Plesset perturbation theories" [J. Chem. Phys. **129**, 044112 (2008)], J. Chem. Phys. **130**, 127101 (2009).

[122] I. Duchemin and X. Blase, Separable resolution-of-the-identity with all-electron Gaussian bases: Application to cubic-scaling RPA, J. Chem. Phys. **150**, 174120 (2019).

[123] A. Takatsuka, S. Ten-no, and W. Hackbusch, Minimax approximation for the decomposition of energy denominators in Laplace-transformed Møller–Plesset perturbation theories, J. Chem. Phys. **129**, 044112 (2008).

[124] D. Braess, *Nonlinear Approximation Theory*, Vol. 7 (Springer-Verlag, Berlin, 2011).

[125] GreenX, https://github.com/nomad-coe/greenX.

[126] M. Azizi, J. Wilhelm, D. Golze, M. Giantomassi, R. L. Panadés-Barrueta, F. A. Delesma, A. Buccheri, A. Gulans, P. Rinke, C. Draxl, and X. Gonze, Time-frequency component of the GreenX library: minimax grids for efficient RPA and *GW* calculations, J. Open Source Softw. **8**, 5570 (2023).

[127] V. Blum, R. Gehrke, F. Hanke, P. Havu, V. Havu, X. Ren, K. Reuter, and M. Scheffler, *Ab initio* molecular simulations with numeric atom-centered orbitals, Comput. Phys. Commun. **180**, 2175 (2009).

[128] T. D. Kühne, M. Iannuzzi, M. Del Ben, V. V. Rybkin, P. Seewald, F. Stein, T. Laino, R. Z. Khaliullin, O. Schütt, F. Schiffmann *et al.*, CP2K: An electronic structure and molecular dynamics software package - Quickstep: Efficient and accurate electronic structure calculations, J. Chem. Phys. **152**, 194103 (2020).

[129] X. Gonze, B. Amadon, G. Antonius, F. Arnardi, L. Baguet, J.-M. Beuken, J. Bieder, F. Bottin, J. Bouchet, E. Bousquet *et al.*, The ABINIT project: Impact, environment and recent developments, Comput. Phys. Commun. **248**, 107042 (2020).

[130] A. H. Romero, D. C. Allan, B. Amadon, G. Antonius, T. Applencourt, L. Baguet, J. Bieder, F. Bottin, J. Bouchet, E. Bousquet *et al.*, ABINIT: Overview and focus on selected capabilities, J. Chem. Phys. **152**, 124102 (2020).

[131] O. Gunnarsson and B. I. Lundqvist, Exchange and correlation in atoms, molecules, and solids by the spin-density-functional formalism, Phys. Rev. B **13**, 4274 (1976).

[132] N. E. Dahlen, R. van Leeuwen, and U. von Barth, Variational energy functionals of the Green function and of the density tested on molecules, Phys. Rev. A **73**, 012511 (2006).

[133] J. F. Dobson and M. P. Das, Topics in condensed matter physics (Nova, New York, 1994), pp. 1–21.

[134] S. L. Adler, Quantum theory of the dielectric constant in real solids, Phys. Rev. **126**, 413 (1962).

[135] N. Wiser, Dielectric constant with local field effects included, Phys. Rev. **129**, 62 (1963).

[136] W. Hackbusch, Computation of best L^∞ exponential sums for $1/x$ by Remez' algorithm, Comput. Visual Sci. **20**, 1 (2019).

[137] W. H. Press, S. A. Teukolsky, W. T. Vetterling, and B. P. Flannery, *Numerical Recipes, 3rd edition: The Art of Scientific Computing* (Cambridge University Press, Cambridge, 2007).

[138] M. Del Ben, O. Schütt, T. Wentz, P. Messmer, J. Hutter, and J. VandeVondele, Enabling simulation at the fifth rung of DFT: Large scale RPA calculations with excellent time to solution, Comput. Phys. Commun. **187**, 120 (2015).

[139] M. Schreiber, M. R. Silva-Junior, S. P. A. Sauer, and W. Thiel, Benchmarks for electronically excited states: CASPT2, CC2, CCSD, and CC3, J. Chem. Phys. **128**, 134110 (2008).

[140] L. Himanen, A. Geurts, A. S. Foster, and P. Rinke, Data-driven materials science: Status, challenges, and perspectives, Adv. Sci. **6**, 1900808 (2019).

[141] L. M. Ghiringhelli, C. Baldauf, T. Bereau, S. Brockhauser, C. Carbogno, J. Chamanara, S. Cozzini, S. Curtarolo, C. Draxl, S. Dwaraknath *et al.*, Shared metadata for data-centric materials science, Sci. Data **10**, 626 (2023).

[142] M. Azizi, J. Wilhelm, D. Golze, F. A. Delesma, P. Rinke, M. Giantomassi, and X. Gonze, Nomad repository *GW and RPA Calculations Using Minimax Grids Provided by Green-X Library* (2024).

[143] J. L. Whitten, Coulombic potential energy integrals and approximations, J. Chem. Phys. **58**, 4496 (1973).

[144] B. I. Dunlap, J. W. D. Connolly, and J. R. Sabin, On some approximations in applications of $X\alpha$ theory, J. Chem. Phys. **71**, 3396 (1979).

[145] J. W. Mintmire, J. R. Sabin, and S. B. Trickey, Local-density-functional methods in two-dimensionally periodic systems. Hydrogen and beryllium monolayers, Phys. Rev. B **26**, 1743 (1982).

[146] O. Vahtras, J. Almlöf, and M. Feyereisen, Integral approximations for LCAO-SCF calculations, Chem. Phys. Lett. **213**, 514 (1993).

[147] X. Ren, P. Rinke, V. Blum, J. Wieferink, A. Tkatchenko, A. Sanfilippo, K. Reuter, and M. Scheffler, Resolution-of-identity approach to Hartree–Fock, hybrid density functionals, RPA, MP2 and *GW* with numeric atom-centered orbital basis functions, New J. Phys. **14**, 053020 (2012).

[148] A. C. Ihrig, J. Wieferink, I. Y. Zhang, M. Ropo, X. Ren, P. Rinke, M. Scheffler, and V. Blum, Accurate localized resolution of identity approach for linear-scaling hybrid density functionals and for many-body perturbation theory, New J. Phys. **17**, 093020 (2015).

[149] X. Ren, F. Merz, H. Jiang, Y. Yao, M. Rampp, H. Lederer, V. Blum, and M. Scheffler, All-electron periodic G_0W_0 implementation with numerical atomic orbital basis functions: Algorithm and benchmarks, Phys. Rev. Mater. **5**, 013807 (2021).

[150] R. A. Kendall, T. H. Dunning, and R. J. Harrison, Electron affinities of the first row atoms revisited. Systematic basis sets and wave functions, J. Chem. Phys. **96**, 6796 (1992).

[151] S. Goedecker, M. Teter, and J. Hutter, Separable dual-space Gaussian pseudopotentials, Phys. Rev. B **54**, 1703 (1996).

[152] G. Lippert, J. Hutter, and M. Parrinello, The Gaussian and augmented-plane-wave density functional method for *ab initio* molecular dynamics simulations, Theor. Chem. Acc. **103**, 124 (1999).

[153] F. Weigend, F. Furche, and R. Ahlrichs, Gaussian basis sets of quadruple zeta valence quality for atoms H–Kr, J. Chem. Phys. **119**, 12753 (2003).

[154] C. Hättig, Optimization of auxiliary basis sets for RI-MP2 and RI-CC2 calculations: Core valence and quintuple-zeta basis sets for H to Ar and QZVPP basis sets for Li to Kr, Phys. Chem. Chem. Phys. **7**, 59 (2005).

[155] J. VandeVondele and J. Hutter, Gaussian basis sets for accurate calculations on molecular systems in gas and condensed phases, J. Chem. Phys. **127**, 114105 (2007).

[156] Y. Jung, A. Sodt, P. M. Gill, and M. Head-Gordon, Auxiliary basis expansions for large-scale electronic structure calculations, Proc. Natl. Acad. Sci. USA **102**, 6692 (2005).

[157] D. Golze, N. Benedikter, M. Iannuzzi, J. Wilhelm, and J. Hutter, Fast evaluation of solid harmonic Gaussian integrals for local resolution-of-the-identity methods and range-separated hybrid functionals, J. Chem. Phys. **146**, 034105 (2017).

[158] Libint, A library for the evaluation of molecular integrals of operators over Gaussian functions, https://github.com/evaleev/libint.

[159] H. J. Vidberg and J. W. Serene, Solving the Eliashberg equations by means of *N*-point Padé approximants, J. Low Temp. Phys. **29**, 179 (1977).

[160] D. R. Hamann, Optimized norm-conserving Vanderbilt pseudopotentials, Phys. Rev. B **88**, 085117 (2013).

[161] M. J. van Setten, M. Giantomassi, E. Bousquet, M. J. Verstraete, D. R. Hamann, X. Gonze, and G.-M. Rignanese, The PSEUDODOJO: Training and grading a 85 element

optimized norm-conserving pseudopotential table, Comput. Phys. Commun. **226**, 39 (2018).

[162] P. Carrier, S. Rohra, and A. Görling, General treatment of the singularities in Hartree-Fock and exact-exchange Kohn-Sham methods for solids, Phys. Rev. B **75**, 205126 (2007).

[163] S. Baroni and R. Resta, *Ab initio* calculation of the macroscopic dielectric constant in silicon, Phys. Rev. B **33**, 7017 (1986).

[164] F. A. Delesma, M. Leucke, D. Golze, and P. Rinke, Benchmarking the accuracy of the separable resolution of the identity approach for correlated methods in the numeric atom-centered orbitals framework, J. Chem. Phys. **160**, 024118 (2024).

[165] See Supplemental Material at http://link.aps.org/supplemental/10.1103/PhysRevB.109.245101 for the raw data of RPA and *GW* calculations.

[166] S. Shabani, D. Halbertal, W. Wu, M. Chen, S. Liu, J. Hone, W. Yao, D. N. Basov, X. Zhu, and A. N. Pasupathy, Deep moiré potentials in twisted transition metal dichalcogenide bilayers, Nat. Phys. **17**, 720 (2021).

[167] K. F. Mak and J. Shan, Semiconductor moiré materials, Nat. Nanotechnol. **17**, 686 (2022).

[168] D. Huang, J. Choi, C.-K. Shih, and X. Li, Excitons in semiconductor moiré superlattices, Nat. Nanotechnol. **17**, 227 (2022).

[169] M. Camarasa-Gómez, A. Ramasubramaniam, J. B. Neaton, and L. Kronik, Transferable screened range-separated hybrid functionals for electronic and optical properties of van der Waals materials, Phys. Rev. Mater. **7**, 104001 (2023).

[170] M. Shishkin and G. Kresse, Implementation and performance of the frequency-dependent *GW* method within the PAW framework, Phys. Rev. B **74**, 035101 (2006).